Redox-Sensitive Cysteines Confer Proximal Control of the Molecular Crowding Barrier in the Nuclear Pore

AUTHOR(S):

Zhang, Wanzhen; Watanabe, Ryuji; Konishi, Hide A.; Fujiwara, Takahiro; Yoshimura, Shige H.; Kumeta, Masahiro

CITATION:

Zhang, Wanzhen ...[et al]. Redox-Sensitive Cysteines Confer Proximal Control of the Molecular Crowding Barrier in the Nuclear Pore. Cell Reports 2020, 33(11): 108484.

ISSUE DATE:

2020-12-15

URL:

http://hdl.handle.net/2433/259818

Article

Cell Reports

Redox-Sensitive Cysteines Confer Proximal Control of the Molecular Crowding Barrier in the Nuclear Pore

Graphical Abstract

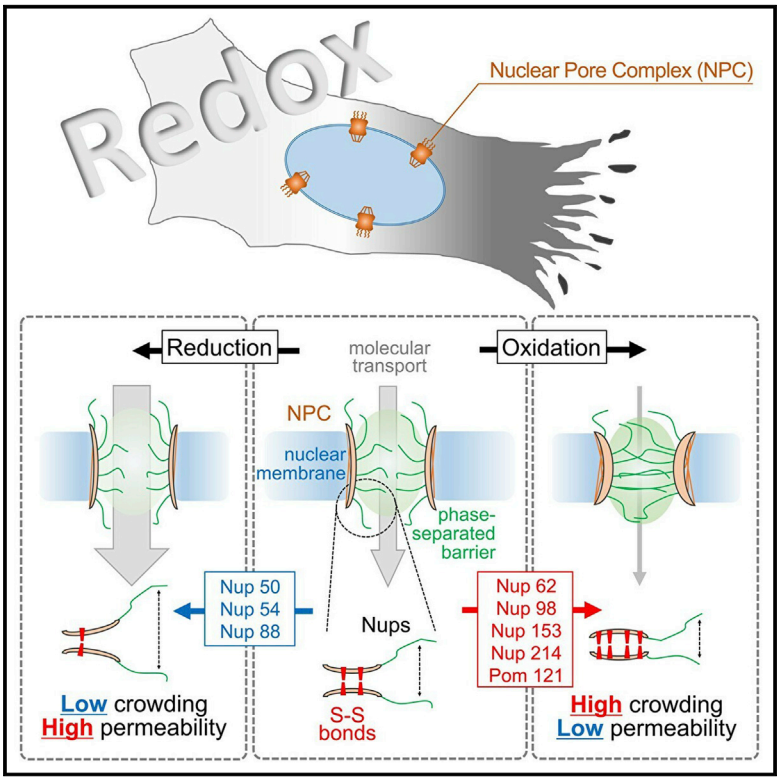

Highlights

- Local molecular crowding within the nuclear pore changes in different redox conditions
- Nucleoporins form disulfide bonds by oxidation and alter the permeability of the pore
- Redox states affect accessibility and retention of cargos to the nuclear pore
- Cysteines at proximal region of nucleoporins confer dynamic control of the pore

Authors

Wanzhen Zhang, Ryuji Watanabe, Hide A. Konishi, Takahiro Fujiwara, Shige H. Yoshimura, Masahiro Kumeta

Correspondence

kumeta@lif.kyoto-u.ac.jp

In Brief

Zhang et al. report the mechanism of redox-sensitive control of molecular crowding barrier in the nuclear pore. Cysteine residues at the proximal region of nuclear pore subunits form disulfide bonds under oxidative stress and decrease the nuclear permeability by altering accessibility and retention of cargos to the nuclear pore.

Zhang et al., 2020, Cell Reports *33*, 108484
December 15, 2020
https://doi.org/10.1016/j.celrep.2020.108484

CellPress

Cell Reports

CellPress OPEN ACCESS

Article

Redox-Sensitive Cysteines Confer Proximal Control of the Molecular Crowding Barrier in the Nuclear Pore

Wanzhen Zhang,[1] Ryuji Watanabe,[1] Hide A. Konishi,[1,3] Takahiro Fujiwara,[2] Shige H. Yoshimura,[1] and Masahiro Kumeta[1,4,*]

[1]Graduate School of Biostudies, Kyoto University, Kyoto 606-8501, Japan
[2]Institute for Integrated Cell-Material Sciences (WPI-iCeMS), Kyoto University, Kyoto 606-8501, Japan
[3]Laboratory of Chromosome and Cell Biology, The Rockefeller University, New York, NY 10065, USA
[4]Lead Contact
*Correspondence: kumeta@lif.kyoto-u.ac.jp
https://doi.org/10.1016/j.celrep.2020.108484

SUMMARY

The nuclear pore complex forms a highly crowded selective barrier with intrinsically disordered regions at the nuclear membrane to coordinate nucleocytoplasmic molecular communications. Although oxidative stress is known to alter the barrier function, the molecular mechanism underlying this adaptive control of the nuclear pore complex remains unknown. Here we uncover a systematic control of the crowding barrier within the nuclear pore in response to various redox environments. Direct measurements of the crowding states using a crowding-sensitive FRET (Förster resonance energy transfer) probe reveal specific roles of the nuclear pore subunits that adjust the degree of crowding in response to different redox conditions, by adaptively forming or disrupting redox-sensitive disulfide bonds. Relationships between crowding control and the barrier function of the nuclear pore are investigated by single-molecular fluorescence measurements of nuclear transport. Based on these findings, we propose a proximal control model of molecular crowding *in vivo* that is dynamically regulated at the molecular level.

INTRODUCTION

As one of the largest protein complexes and the solo guardian of extensive nucleocytoplasmic exchanges, the nuclear pore complex (NPC) plays an indispensable role in cells. It comprises more than 30 different subunits called nucleoporins (Nups); these Nups are assembled into an 8-fold symmetric structure, with the central channel sandwiched by cytoplasmic and nuclear rings (Lin et al., 2016). Nucleocytoplasmic molecular transport is achieved through the central channel of the NPC, where intrinsically disordered regions (IDRs) of the pore-forming Nups are concentrated and serve as the selective barrier (Tetenbaum-Novatt and Rout, 2010). At the primary level of control, small molecules (<40 kDa) can diffuse passively through NPCs, whereas large molecules (>40 kDa) without the coordination of nuclear transport receptors (TRs) are excluded from the NPC (Elad et al., 2009; Mohr et al., 2009).

The IDR-containing Nups that are involved in transport control are especially enriched in hydrophobic phenylalanine-glycine (FG) repeat motifs (Denning et al., 2003; Frey and Görlich, 2007). Many studies suggested that the highly crowded molecular environment within the central channel of the NPC is responsible for its barrier function (Grünwald and Singer, 2012; Lim et al., 2007). This highly dynamic environment of the crowded FG-repeats is considered to be the main factor determining the size-limited diffusion barrier within the NPCs (Timney et al., 2016). Moreover, FG repeats can provide concentrated interaction sites within the NPCs, which are crucial for TR-related nuclear transport (Aramburu and Lemke, 2017; Li et al., 2016; Otsuka et al., 2008; Raveh et al., 2016). However, due to the lack of experimental methods to directly measure molecular crowding states in intact nuclear pores, much of our current understanding of the crowding barrier is derived from *in vitro* experiments or *in silico* theoretical and computational modeling (Zilman, 2018). We have previously established a method to measure crowding states within the NPC using a crowding-sensitive molecular probe (Konishi et al., 2017; Morikawa et al., 2016) and revealed that the central channel of NPCs contains highly crowded FG-Nups at both the cytoplasmic and the nucleoplasmic sides of the pore, with a less crowded central cavity under physiological conditions.

At the same time, different lines of investigation showed that oxidative stress has a direct effect on nuclear transport activity, and multiple FG-Nups are involved in this stress response (Crampton et al., 2009; Patel and Chu, 2011). We have previously reported that permeability of the nuclear pore is generally decreased by oxidative stress, which is accompanied by the formation of disulfide bonds among Nups (Yoshimura et al., 2013). Other transport-related factors, such as nuclear localization signals (NLSs) (García-Yagüe et al., 2013) and TRs (Hakim et al., 2013), also showed aberrant nuclear transport under oxidative stress. Although several Nups are quite enriched in

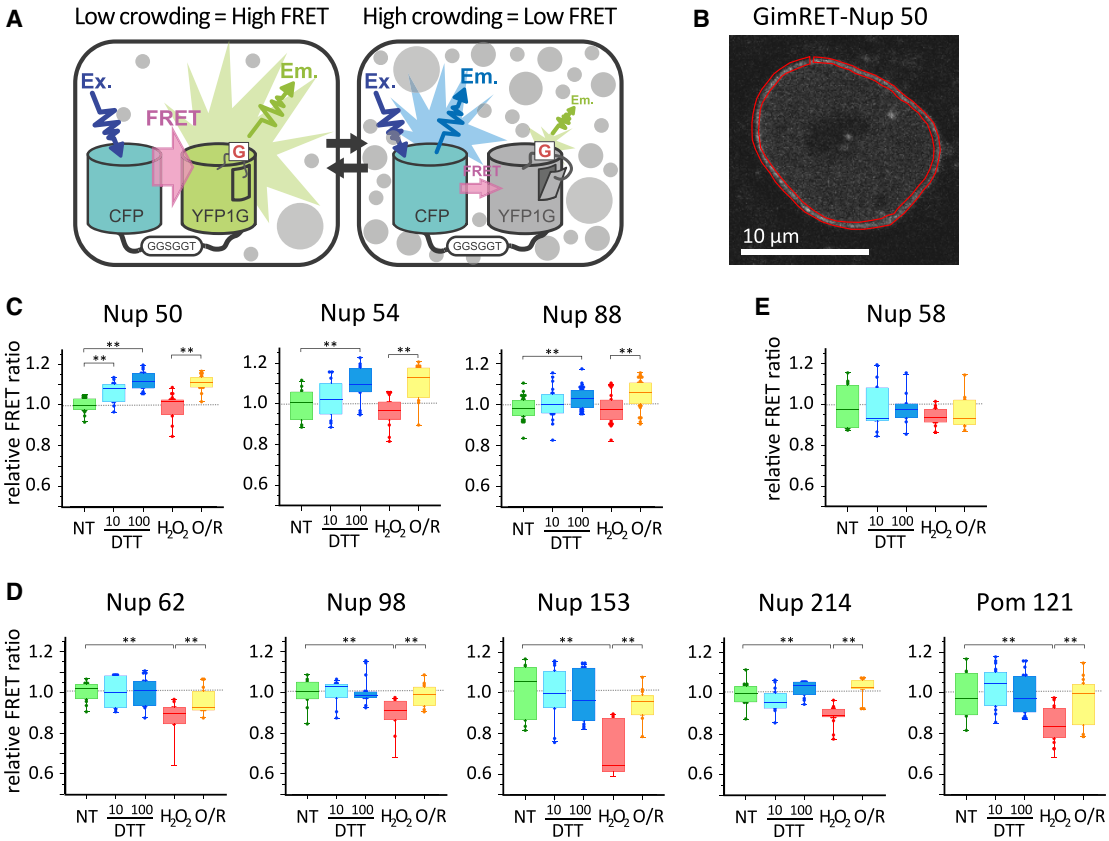

Figure 1. Crowding States of Individual Nups under Redox Conditions

(A) Schematic illustration of the crowding-sensitive FRET probe GimRET. Due to the collapse of the acceptor fluorescent protein, GimRET shows low FRET in a highly crowded environment.

(B) HeLa cells expressing Nups fused to crowding-sensitive probe GimRET were semi-permeabilized by digitonin treatment and observed by fluorescence microscopy. The entire nuclear envelope region was selected (indicate by red line) for bulk FRET ratio analysis.

(C–E) Bulk analysis of relative FRET ratios of GimRET-Nups expressed in digitonin-treated HeLa cells under standard conditions (green), reducing conditions (10 and 100 mM DTT treatment, blue), oxidative conditions (2 mM H_2O_2 treatment, red), and successive oxidative stress (2 mM H_2O_2) and reducing (100 mM DTT) conditions (O/R) to assess recovery (yellow) (*$p < 0.05$, **$p < 0.01$, by Welch's t test). Nups tested were classified into three categories: DTT-sensitive Nups (Nup 50, Nup 54, and Nup 88), H_2O_2-sensitive Nups (Nup 62, Nup 98, Nup 153, Nup 214, and Pom 121), and unresponsive Nup 58, respectively.

cysteine (Figure S1), the role of disulfide bond formation in controlling NPC permeability largely remains unknown.

To understand how the molecular crowding state is dynamically controlled, we directly measured the crowding states of Nups under different redox conditions, using a crowding-sensitive FRET (Förster resonance energy transfer) probe, GimRET. To link the crowding control to the function of the NPC, we analyzed nuclear transport events at the single molecular level. Based on these findings, we propose a model of *in vivo* molecular crowding control that is achieved by bundling proximal regions of the crowding molecules.

RESULTS

Dynamic Regulation of Molecular Crowding States in Different Redox Conditions

We have previously established a method to monitor local molecular crowding states around specific Nups using a crowding-sensitive FRET probe, GimRET (Konishi et al., 2017). Due to the collapse of the acceptor fluorescent protein in a highly crowded environment, this FRET probe yields lower FRET ratios with increasing crowding (Figure 1A) (Morikawa et al., 2016). A set of Nups from cytoplasmic, nucleoplasmic, central channel, and membrane-associated scaffold regions of the NPC was chosen for the crowding assay. HeLa cells were transfected with plasmids to express the respective Nups fused with GimRET. All the GimRET-fused Nups used in this research were correctly localized to the nuclear envelope (Figures S2A–S2C) (Konishi et al., 2017). To analyze the change in their crowding states under oxidative stress, we incubated the cultured cells with 2 mM H_2O_2 for 1 h. H_2O_2-stressed cells and non-stressed cells were subsequently treated with digitonin to permeabilize the plasma membrane and were observed under the confocal microscope. To measure the crowding states under reduced conditions, we treated permeabilized non-stressed cells with 10 or 100 mM dithiothreitol (DTT). Because GimRET FRET signal showed a weak negative correlation with its expression level, cells with a similar level of expression were analyzed to obtain

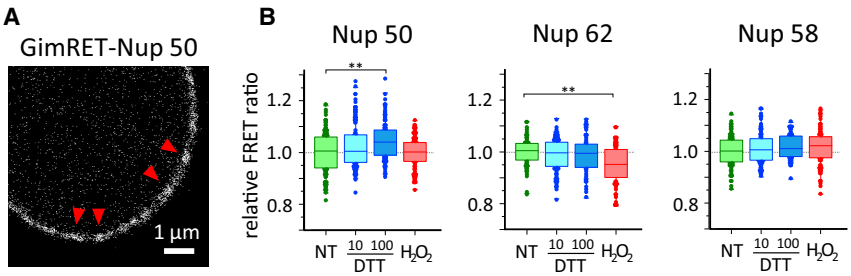

Figure 2. Crowding States of Individual Nups at the Single-NPC Level

(A) GimRET measurements were performed at the single-NPC level. HeLa cells were transfected with plasmids to express GimRET-fused Nups 50, 58, and 62, semi-permeabilized by digitonin, and observed under a microscope. In the example shown, GimRET-Nup 50 signals on the nuclear envelope were observed without oxidative stress. Fluorescent spots corresponding to single NPCs are indicated with red arrowheads. The detailed procedure for the image analysis is described in the Supplemental Information.

(B) Results of the single-NPC-level analysis of relative FRET ratios for Nup-GimRET-expressing HeLa cells under standard conditions (green), reducing conditions (blue), and oxidative conditions (red) (*$p < 0.05$, **$p < 0.01$, by Welch's t test).

comparable data (Figure S2D). Neither H_2O_2 nor DTT treatments altered the localization of GimRET-fused Nups in our experimental condition (Figures S2E and S2F).

Quantitative analysis of the FRET signals at the nuclear envelope (Figure 1B) clearly revealed differential responses among Nups. In response to the DTT treatments, Nups 50, 54, and 88 showed significant increases in the FRET ratio, which indicates a decrease in the molecular crowding (Figure 1C). In contrast, the crowding state of these Nups did not change in response to H_2O_2 treatment; moreover, a successive treatment with H_2O_2 followed by 100 mM DTT showed a final crowding state equivalent to 100 mM DTT treatment alone. In contrast, Nups 62, 98, 153, and 214 and Pom 121 exhibited a significant decrease in the FRET ratio in response to H_2O_2 treatment, but none of these showed a change in the FRET ratio in response to DTT treatment (Figure 1D). When the cells were treated successively with H_2O_2 followed by 100 mM DTT, the crowding states of these Nups were restored to the non-treated level. A sulfhydryl-reactive oxidant diethylmaleate (DEM) also decreased the FRET ratio of these Nups (Figures S3A and S3B), indicating that increase in the crowding status was due to the formation of disulfide bonds at cysteine residues. Of the nine Nups that were tested, all but one were selectively sensitive to either oxidizing or reducing conditions, altering the degree of crowding by either increasing crowding in oxidizing conditions or decreasing crowding in reducing conditions. Only Nup 58 failed to show a change in the FRET ratio for any redox condition tested (Figure 1E).

To gain further insight into the control of crowding within individual NPCs facing altered redox conditions, we performed GimRET measurements at the single-NPC level, as described in STAR Methods. Fluorescent spots on the nuclear membrane, which were assumed to derive from a single NPC, were recorded and statistically analyzed (Figure 2A). Accuracy of the single-NPC detection was evaluated by overlaying immunostaining of the NPC and was evaluated to be 92.0% (Figure S2E). More than 50 spots were analyzed for Nups 50, 62, and 58 in each redox condition. Statistical analyses showed crowding changes that were consistent with the bulk-level analysis (Figure 2B). The apparent degrees of response were smaller in the single-NPC analyses compared with the bulk assays (Figures 1C–1E) due to the limitation in detecting a single NPC. NPCs with stronger CFP signal were picked up in the single-NPC analyses, which showed lower FRET signal (Figure S2D), resulting in selecting highly crowded NPCs in this analysis.

Overall, both bulk and single-NPC-level GimRET analyses suggested that specific Nups possess intrinsic crowding control mechanisms to counter environmental changes. Some Nups, including Nups 50, 54, and 88, are sensitive to a reducing environment, while others, including Nups 62, 98 153, and 214 and Pom 121, contribute to increased molecular crowding in response to oxidative stress. However, depending on their location and function within the NPC, some Nups, such as Nup 58, might be insensitive to changes in redox conditions. These results suggest that there may be three types of Nups within the NPC: oxidation-sensitive Nups, reduction-sensitive Nups, and invariant Nups. Barrier function of the NPC might be regulated by adaptive crowding control, which is mediated by the formation or disruption of redox-sensitive disulfide bonds between Nups.

Adaptive Crowding Control Is Achieved by Disulfide Bond Formation

We have previously shown that certain Nups form disulfide bond(s) in an oxidative environment (Yoshimura et al., 2013). Cysteine residues in Nups are mostly found in non-IDR regions within the proteins (Figures 3A and S1). To understand the relationships between disulfide bond formation and redox-mediated crowding in the NPC, several cysteine-to-serine (CS) mutations were introduced to GimRET-Nup constructs. The effect of the mutations was analyzed by the single-NPC-level GimRET measurement.

Nup 62 contains two cysteines (C478 and C509) in its carboxyl end. Replacement of these two cysteine residues to serines did not change the localization of Nup 62 in cells (Figure 3B). However, compared with wild-type (WT) Nup 62, the CS mutant showed no FRET signal decrease in response to oxidative stress (Figure 3C), which suggests that the CS mutant lost its specific crowding control in response to oxidative conditions. In contrast, Nup 153 contains 28 cysteine residues, and among these, 21 cysteine residues are clustered in the middle part of the molecule, mostly located within the zinc-finger region (residues 658–885) (Partridge and Schwartz, 2009). These cysteine residues (21 cysteine residues between C585 and C874) were mutated to serines. HeLa cells expressing this Nup 153 CS mutant showed correct localization of the mutant protein (Figure 3D). However, similar to the CS mutant of Nup 62, the Nup 153 CS mutant also lost adaptive crowding control, because there was no difference in its FRET signal with or without

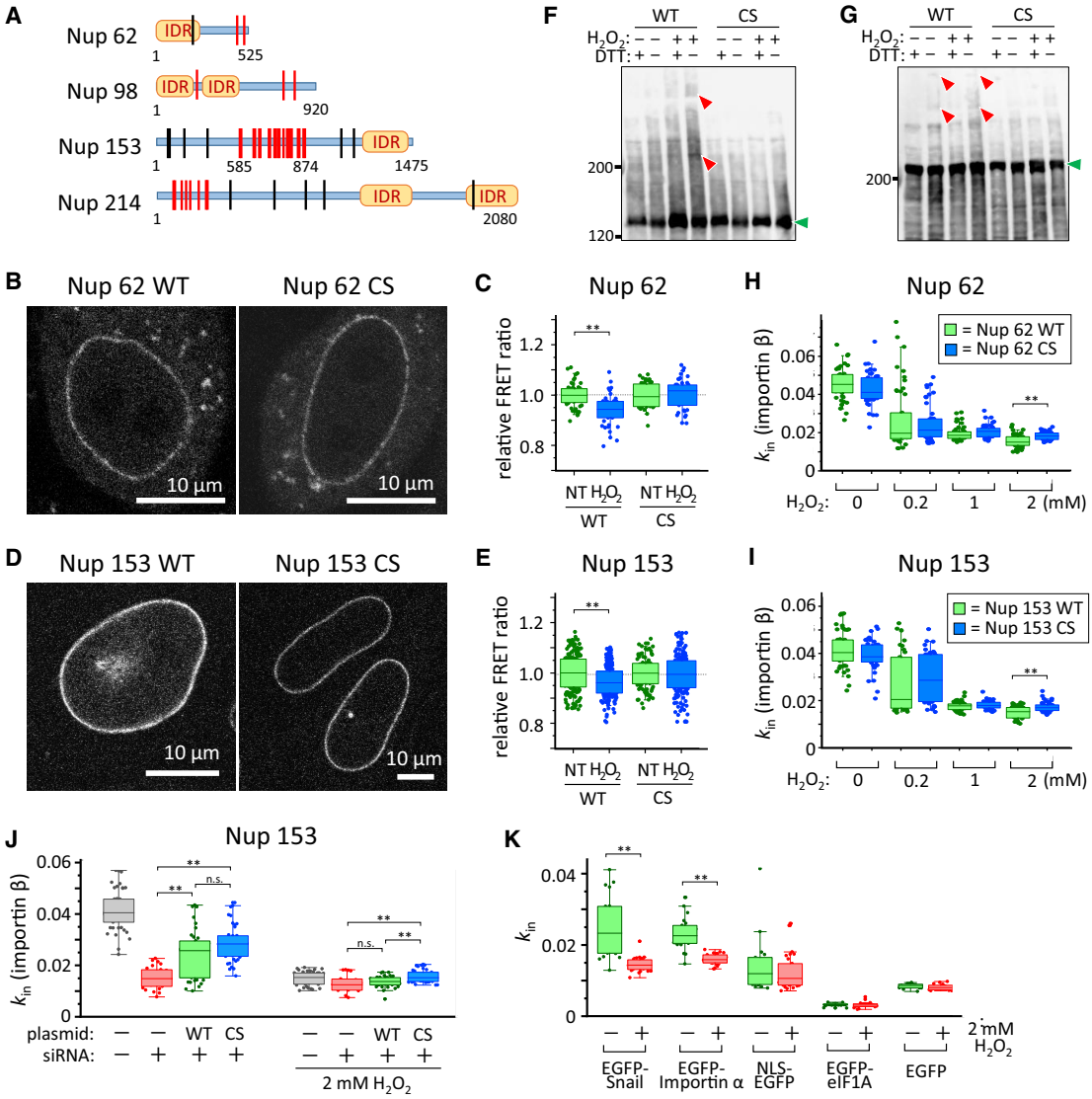

Figure 3. Cysteine Residues in H_2O_2-Sensitive Nups Are Involved in Disulfide Bond Formation and Nuclear Transport Control

(A) A map of cysteine localizations within H_2O_2-sensitive Nups. Intrinsically disordered regions (IDRs) are shown in yellow boxes. Cysteine residues are indicated with vertical lines; cysteine residues replaced by serine are indicated with red lines.

(B and D) Subcellular localization of Nup 62 and 153 wild-type (WT) and respective cysteine-to-serine (CS) mutants in intact cells. Both CS mutants showed similar localizations to WT.

(C and E) Single-NPC-level GimRET analysis of digitonin-treated HeLa cells expressing WT or CS mutant Nup 62 and Nup 153, respectively, under non-treated conditions (green) and 2 mM H_2O_2 treatment (blue) (**$p < 0.01$, by Welch's t test).

(F and G) Western blot analysis of HeLa cells expressing WT or CS mutants of Nup 62 or Nup 153, either non-treated ($-H_2O_2$) or exposed to 2 mM H_2O_2 ($+H_2O_2$); the nuclei were collected and prepared for western blot analyses in the absence (−DTT) or presence (+DTT) of 100 mM DTT. Immunoblotting was performed using antibodies against GFP to detect GimRET-fused Nups. Slow-migrating bands (red arrowheads) and bands at the expected positions (green arrowheads) are indicated.

(H and I) Statistical analysis of the FRAP recovery rate of nucleoplasmic mCherry-fused importin β1 observed in live HeLa cells expressing WT and CS mutants of Nup 62 and Nup 153, respectively, at 37°C. The averaged k_{in} for measurements under the non-treated condition (0 mM) and different concentrations of H_2O_2 (0.2, 1, and 2 mM) are presented (**$p < 0.01$, by Welch's t test).

(J) Import rates of mCherry-fused importin β measured by FRAP analyses in HeLa cells transfected with siRNA against Nup 153 and plasmid to express siRNA-resistant Nup 153 WT and CS mutant (**$p < 0.01$, by Welch's t test).

(K) Nuclear import rates obtained by the FRAP analyses of EGFP-Snail, EGFP-Importin α, NLS-EGFP, EGFP-eIF1A, and EGFP expressed in HeLa cells in the presence/absence of 2 mM H_2O_2 (**$p < 0.01$, by Welch's t test).

n.s., no significant differences.

oxidative stress (Figure 3E). Subcellular localization of the CS mutants was not changed in normal and H_2O_2-treated cells (Figures S3C and S3D), suggesting the cysteine-dependent crowding control occurred within the nuclear pore.

Stress-induced disulfide bond formation was also analyzed by western blot analyses. When WT GimRET-fused Nup 62 or 153 was expressed and detected in a DTT-free western blot, slow-migrating bands were detected in the H_2O_2-treated samples (Figures 3F and 3G, red arrowheads). The amount of slow-migrating band (red arrowheads) to the monomeric one (green arrowheads) was increased from 6.9% to 31.8% for Nup 62 and from 4.8% to 8.3% for Nup 153 by H_2O_2 treatment, respectively, which indicates the formation of an inter-molecular disulfide bridging (Yoshimura et al., 2013). The slow-migrating bands were not detected when the samples were treated with DTT because of the breakage of the bonds. When CS-mutated GimRET-Nups 62 and 153 were analyzed in the same way, the slow-migrating bands were not detected, even in the H_2O_2-treated samples. Taken together with the FRET measurements, these findings revealed that cysteine residues play a direct and essential role in oxidative stress-induced adaptive crowding control through the formation of disulfide bonds.

We extended our mutation analysis to other Nups and noted that CS mutations often resulted in mislocalization of the respective Nup. For example, when three CS mutations, C188S (located within GLEBS [Gle2-binding-sequence domain]), C743S, and C818S (autoproteolytic region), were introduced into Nup 98 (Ren et al., 2010), its localization at the nuclear envelope was abolished (Figure S3E). A similar result was obtained for Nup 214. Among 13 cysteine residues in Nup 214, 8 of them (C102, C110, C168, C186, C199, C231, C294, and C298) are clustered at the N-terminal region, within β-propeller blades (Napetschnig et al., 2007). When all eight cysteines were mutated to serines, the nuclear envelope localization was abolished (Figure S3F), demonstrating the role of cysteines in the proper molecular targeting of these Nups within the pore.

The Degree of Crowding Is Directly Linked to the Permeability of the NPC

We next asked whether the degree of crowding and the permeability of the nuclear pore were inversely correlated, using fluorescence recovery after photobleaching (FRAP) analysis of a major TR, importin β1. HeLa cells transiently co-expressing mCherry-fused importin β1 and EGFP-fused Nup 62 or 153 (both WT and CS mutant versions of both proteins) were used. Steady-state localization of importin β1 was not altered by the expression of the CS mutant Nups (Figure S4A). The relative amount of respective EGFP-fused Nups to the endogenous ones were 1.39 and 1.48 for WT and CS Nup 62 and 1.35 and 1.05 for WT and CS Nup 153, as estimated by western blot analysis (Figure S4B). FRAP measurement was performed by bleaching the mCherry-Importin β1 signal throughout the nucleoplasmic area of pEGFP-Nup-expressing cells (Figure S4C), and the fluorescence recovery within the nucleoplasm was analyzed. Relative nuclear transport rate constants (k_{in}) under different concentrations of H_2O_2 were obtained by curve fitting. In response to treatment with 2 mM H_2O_2, HeLa cells expressing the Nup 62 or Nup 153 CS mutant showed a higher k_{in} compared with those expressing the respective WT Nups (Figures 3H and 3I). To further elucidate the effect of the CS mutations, we tested a combination of siRNA knockdown and exogenous gene expression of siRNA-resistant Nup 153. Under this rescue condition, endogenous Nup 153 was suppressed to be 25%–27% and was replaced to 82% and 90% of WT and CS mutant Nup 153, respectively (Figures S4D and S4E). The FRAP analyses of importin β1 in these cells revealed that knockdown of Nup 153 drastically decreased the import rate, the effect of which was partly rescued by introducing exogenous Nup 153, both WT and CS mutant, to similar levels (Figure 3J). When treated with 2 mM H_2O_2, the CS mutant failed to restrain importin β1 dynamics. These results clearly demonstrated the role of disulfide bonds in the regulation of NPC permeability.

Effects of the permeability control on other nuclear shuttling molecules were further analyzed. EGFP-fused Snail (direct cargo for importin β1), EGFP-importin α, NLS-EGFP, EGFP-eIF1A (NLS-dependent import cargo), and EGFP were expressed in HeLa cells, and the nuclear import rates were analyzed by the FRAP analyses under both normal and 2 mM H_2O_2-treated conditions. Both Snail and importin α showed significant decrease in their import rates under oxidative stress, as was the case with importin β1 (Figure 3K). However, nuclear transport dynamics of NLS-cargos and passively diffusing molecule were not affected by the stress. These results suggest that redox-dependent crowding control potentially affects a broad range of nuclear shuttling molecules, especially when the NPC translocation step serves as the late limiting step for their nuclear accumulation.

To understand the adaptive changes of the nuclear transport dynamics at the single-NPC level, we set up a single-molecule fluorescence observation system. A total internal reflection fluorescence (TIRF) microscope was used in the highly inclined thin illumination (HILO) mode by adjusting the incidence angle of the excitation laser (Figure 4A) (Tokunaga et al., 2008). Human importin β1 was expressed in bacteria, purified, and labeled with tetramethyl rhodamine (TMR). Digitonin-treated HeLa cells were incubated with 1 nM TMR-importin β1, and the nuclear transport events were recorded at a rate of 15 ms/frame for 60 s (Figure 4B). Retention events of importin β1 on the nuclear membrane were detected as described in STAR Methods, and the activities of each individual NPC were evaluated. A 10 mM DTT condition was set as the control standard to avoid natural oxidation during observation.

With the standard 10 mM DTT condition, for 89 NPCs observed from 10 nuclei measurements, 421 fluorescent spots were successfully detected. Among them, 68.2% (287/421) were detected within a single frame (<15 ms), whereas the remaining 31.8% (134/421) persisted for multi-frames (>15 ms) (Figure 4C, top). Events that persisted more than 150 ms constituted 23.5% of the total (99/421). The events were further analyzed for each individual NPC. The number of detectable events at each NPC during a 60-s observation time frame ranged from 1 to 11 (Figure 4D, top), suggesting the existence of highly permeable NPCs and barely permeable ones. The average number of events in 60 s was 4.7 ± 2.1 (Figure 4E, top).

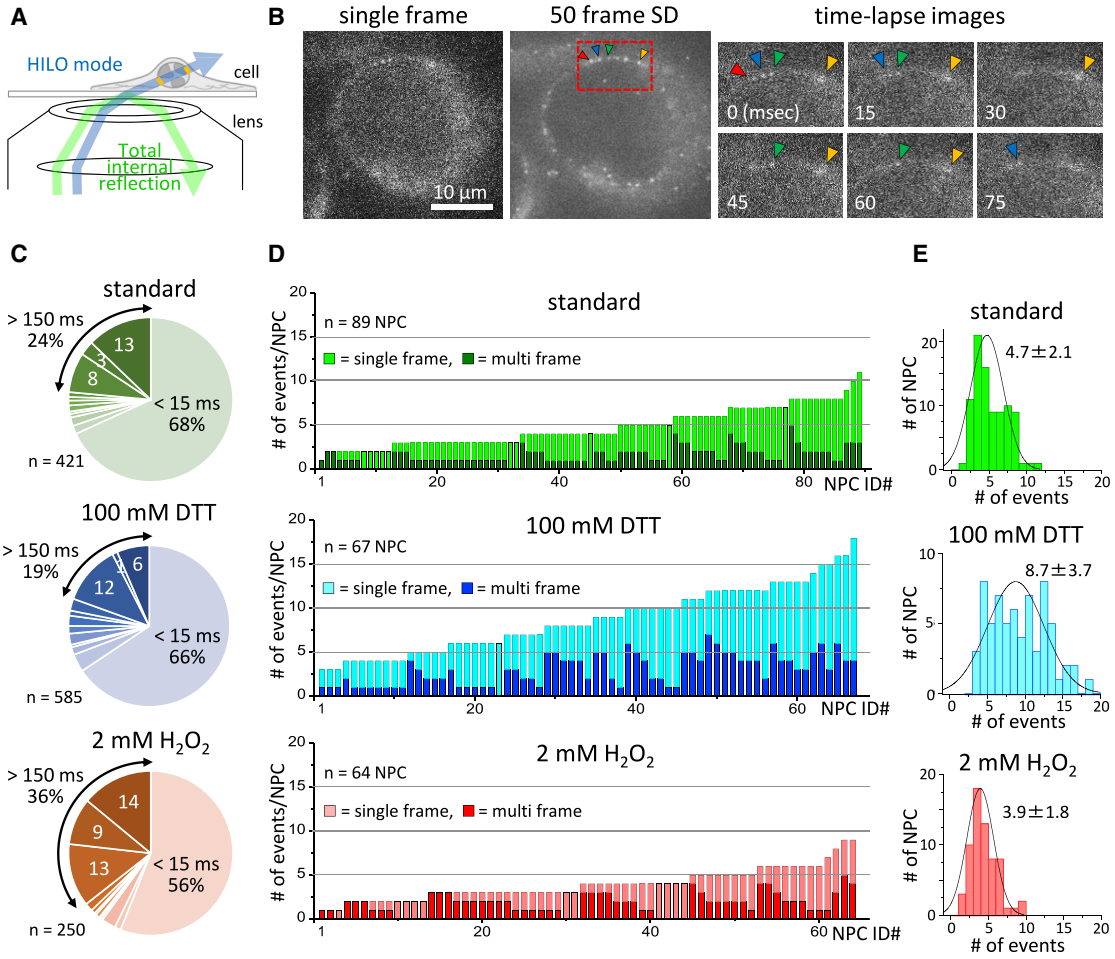

Figure 4. Nuclear Transport Dynamics at the Single-NPC Level under Different Redox Conditions

(A) Microscope setup for single-molecule fluorescence observations using a total internal reflection fluorescence (TIRF) microscope. The highly inclined thin illumination (HILO) mode was set up by adjusting the angle of incidence of the excitation laser to dissect the nucleus.

(B) Permeabilized HeLa cells were incubated with 1 nM TMR-Importin β1. The nuclear transport events were recorded by detecting fluorescent spots on the nuclear envelope every 15 ms for 60 s at room temperature. The position of the NPC was identified by creating standard deviation images from 50 consecutive images. Retention times of fluorescent importin β1 were analyzed based on time-lapse images and quantitative thresholding (described in Supplemental Information).

(C) Quantitative analysis of nuclear transport through NPCs under standard conditions (green), reducing conditions (blue), and oxidative conditions (orange); percentages of short retention (single frame, ≤15 ms) and long retention (sum of 10–49, 50–100, >100 frames, >150 ms) events are shown.

(D) Numbers of events for each NPC in a 60-s observation window under standard conditions (green bars, n = 89 NPCs), reducing conditions (blue bars, n = 67 NPCs), and oxidative conditions (red bars, n = 64 NPCs). The NPC ID numbers were sorted according to the number of events of the measured data. Numbers of single-frame (≤15 ms, light color) and multi-frame (>15 ms, dark color) events for each NPC are shown.

(E) Histogram of the event frequency for each NPC under standard conditions (green), reducing conditions (blue), and oxidative conditions (red), with the Gaussian distribution fitting. Mean ± SD values are presented.

The same single-molecule fluorescence measurement assays were performed under different redox conditions using cells pre-incubated with 2 mM H_2O_2 for 1 h or treated with 100 mM DTT. In these conditions, significant changes in the NPC activity were observed. In total, 250 events in 64 NPCs from 8 nuclei and 585 events in 67 NPCs from 7 nuclei were detected for oxidized and reduced conditions, respectively. In the reducing condition, 65.7% (384/585) of the events occurred during a single frame, but only 56.0% (140/250) of these single-frame events were observed for the oxidizing condition (Figure 4C, middle and bottom); thus, a significantly lower incidence of fast events occurred under the oxidizing condition, compared with either the standard (10 mM DTT) or the reducing conditions (100 mM DTT). Consistent with these observations, the incidence of events that persisted more than 150 ms was significantly higher in the oxidizing condition (35.6%, 89/250), although the proportion of events that persisted more than 150 ms in the strongly reducing condition (19.5%, 114/585) was comparable with the standard condition (23.5%, 99/421). In contrast, the number of transport events per NPC was significantly changed in the reduced condition.

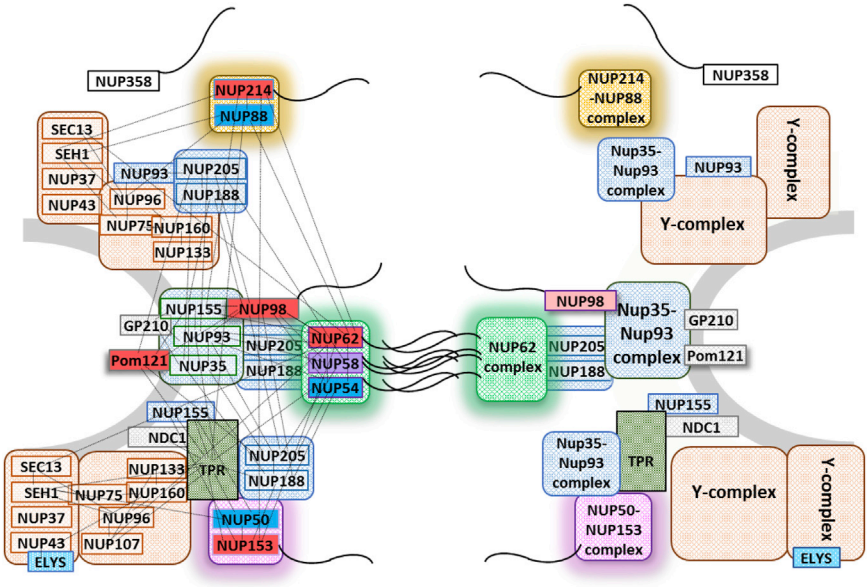

Figure 5. Distribution of Redox-Sensitive Nups in the NPC

Sub-complex structures are shown on the right panel, and detailed constituent Nups in each sub-complex are shown on the left panel, with known interactions (gray lines) identified by cross-linking mass spectrometry (Kim et al., 2018; Kosinski et al., 2016). Nups sensitive to reducing conditions (indicated in blue) and oxidative conditions (red) co-exist within several sub-complex units, and the redox-insensitive Nup 58 is shown in purple.

The events were further analyzed for each individual NPC in both reduced and oxidized conditions (Figure 4D, middle and bottom). In the presence of 100 mM DTT, the number of events for all NPCs ranged from 3 to 19, with an average number of 8.7 ± 3.7, which was significantly higher than that under the standard condition (10 mM DTT); however, in the presence of 2 mM H_2O_2, transport was similar to what we observed for the standard condition: the number of events ranged from 2 to 9, with an average number of 3.9 ± 1.8 (Figure 4E, middle and bottom).

Together, these results revealed how redox conditions affect the nuclear transport at the single-NPC level. Oxidative stress alters the property of the NPC to hold transport molecules longer in the pore and suppress the transport efficiency, while a reducing environment acts on the NPC to render it more accessible for the transport of biomolecules.

DISCUSSION

In this report, we found that individual Nups change their crowding states when facing different redox environments, which affects the permeability of the nuclear pore. Disulfide bonds formed among cysteine residues of Nups were essential regulatory factors in this mechanism. Based on these findings, we propose a model for the dynamic control of molecular crowding, which provides molecular insights into the adaptive control of many phase-separated subcellular compartments *in vivo*.

Adaptive Regulation of Nups Is Coordinated within Sub-complex Structures

As one of the largest subcellular molecular complexes, reaching approximately 110 MDa in total, the NPC is composed of several sub-complexes, such as the Y-complex (Kelley et al., 2015), the Nup 62 sub-complex (Chug et al., 2015), the Nup 98 complex (Ren et al., 2010), and the Nup35 complex (Fischer et al., 2015) (Figure 5). For all the constituent Nups tested, there were always Nups that responded to opposite redox conditions present within the same sub-complex structure: pairing of an H_2O_2-sensitive Nup and a DTT-sensitive Nup, Nups 62 and 54, respectively, in the Nup 62 sub-complex, central channel; Nups 153 and 50, respectively, in a transport partnership in the nuclear basket; and Nups 214 and 88, respectively, in the Nup 214 sub-complex and cytoplasmic filament. This implies a balanced structure comprising constituent Nups within a given sub-complex, which maintains an adaptive potential for redox conditions. These redox-sensitive Nups are distributed in almost every sub-structure of the NPC, including the transmembrane region (Pom 121) and peripheral region on both sides of the pore (Nup 98), suggesting an overall structural adaptation within NPCs to changing redox conditions.

Several Nups in different sub-complexes are known to interact with each other, such as Nup 153 and Nup 50 (Kosako et al., 2009). Because Nup 50 is sensitive to reducing conditions and Nup 153 is sensitive to oxidizing conditions, the adaptive regulation potential within the sub-complex structure may also extend to spatially coordinated partner Nups. Furthermore, it was reported that the binding of importin β1 to NPCs could induce a conformational compaction of Nup 153 (Lim et al., 2007). More recent discoveries revealed that Nup 50 provides direct docking sites for the transport complex (Sun et al., 2013), and an ultrafast interaction occurs between Nup 153 and importin β1 (Milles et al., 2015). All the above-mentioned studies support the notion that Nup 50 and Nup 153 cooperate during the nuclear transport process, with the crowding states adjustable to the particular redox circumstances. The Ran binding activity of the Nup 153 CS mutant was comparable with WT, as revealed by co-precipitation assay (Figure S5A). Several studies revealed that the Zinc-finger domain of Nup153, which is enriched in cysteines, directly binds to Ran-GDP and controls Ran-dependent nuclear transport mediated by importin β (Lowe et al., 2015; Partridge and Schwartz, 2009; Schrader et al., 2008). Although cysteines are suggested to play a supportive role in Nup 153-Ran interaction (Figure S5B), mutation of these cysteines in serines did not significantly affect the Ran binding activity. Therefore, a major cause of the observed effect of Nup 153 CS in this report is suggested to come from disulfide bond formation, rather than the alteration in Ran binding activity. Both crowding degree (Figure 3E) and import rate of importin β1 (Figure 3I) under normal redox

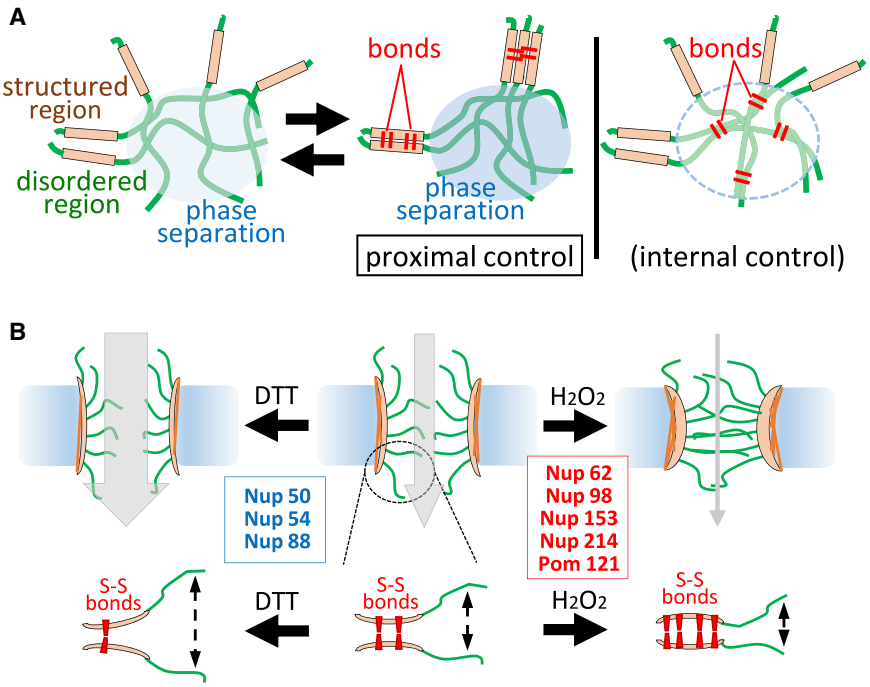

Figure 6. A Model of Proximal Control of Phase Separation *In Vivo*

(A) A general model of dynamic phase-separation control *in vivo* by the proximal regions. Phase separation is maintained by weak and multivalent interactions of the disordered regions in the proteins. To control the nature of the phase separation, the density of the disordered region within the area must be altered seamlessly. Bonding of the structured regions proximal to the disordered regions provides seamless control of the crowding status of disordered regions. Bonding between disordered regions directly restricts the free movement of the peptides; therefore, this internal control is expected to be unsuitable for adaptive regulation of phase separation.

(B) A model of proximal control of phase separation in the NPC. Many Nups contain cysteines in their structured regions. They spontaneously form disulfide bonds and serve as "sensors" for changing redox environments. Under reducing conditions, several Nups, including Nups 50, 54, and 88, sense the environment to weaken the molecular crowding, rendering the NPC more accessible to transport molecules. In oxidizing conditions, disulfide bonds are formed between Nups, including Nups 62, 98, 153, and 214 and Pom 121, to increase the degree of crowding, thereby retaining transport molecules longer in the pore. Therefore, transport activity is enhanced in reducing conditions and suppressed in oxidizing conditions.

conditions are similar for Nup 153 WT and CS-expressing cells, which also supports this idea.

We suggest that both inter- and intra-sub-complex interactions are involved in the redox-dependent crowding control in the NPC. Some key Nups may play central roles in redox sensing and organize a global change of the NPC structure through inter- and intra-sub-complex interactions. Further studies focusing on the molecular interactions between Nups in different redox conditions will reveal the detailed molecular mechanisms underlying the redox response of the NPC.

Proximal Control Model of Molecular Crowding *In Vivo*

Many *in vitro* and *in vivo* experiments suggest that the IDR regions of Nups form a selective barrier based on a phase-separation mechanism in the NPC (Celetti et al., 2020; Frey and Görlich, 2007; Frey et al., 2006; Konishi et al., 2017; Konishi and Yoshimura, 2020). However, most of the cysteine residues found to be involved in crowding control in this study were localized in structured (non-IDR) regions of Nups (Figure 3A). Search for cysteine residues in other Nups also revealed that cysteines tend to be positioned outside of IDR/unstructured domains (Figure S1). Therefore, the crowding control is not simply achieved by direct bonding within the crowding regions, but rather by regulating proximal domains. In addition, many studies have suggested that Nups regulate the curvature of the nuclear membrane directly (Doucet et al., 2015; Mészáros et al., 2015) or cooperatively (Kim et al., 2018; Vollmer et al., 2012), which may contribute to an integral structural adjustment at the whole NPC level. Based on this idea, we propose a proximal control model of molecular crowding *in vivo* (Figure 6A). Phase separation is achieved by weak and multivalent interactions among molecules, rather than strong stereoscopic binding forces. Compared with the internal control, the proximal control system is able to adjust the density of the molecules seamlessly and is therefore more suitable for adaptive regulation of the molecular crowding while maintaining the phase-separated states.

Our results support the model that redox-sensitive control of the molecular crowding in the NPC is achieved by the formation or disruption of disulfide bonds among Nups (Figure 6B). In this case, cysteine residues in the structured region function as a "sensor" for environmental conditions, and the IDR serves as an "effector" that adaptively alters its crowding states to control the barrier function of the NPC. Recently, cysteine residues in structured regions of several IDR-containing proteins, such as heterochromatin protein 1 and gamma-gliadin, were found to play an important role in the liquid-liquid phase-separation process (Sahli et al., 2019; Sanulli et al., 2019). These findings also support our proximal control model of molecular crowding. We found that Nups 62, 98, 153, and 214 and Pom 121 increase their crowding states in an oxidizing environment (Figure 1D), and that the increased crowding is accompanied by the formation of disulfide bonds in Nup 62 and Nup 153 (Figure 3). In addition, we also revealed that other Nups, Nups 50, 54, and 88, sense a reducing environment and decrease their crowding states (Figure 1C). Taking both sets of results into consideration, we posit that some disulfide bonds are pre-established in normal conditions, which may help to maintain the selective barrier. Accordingly, the NPC may possess a broad range of adaptations to changing redox conditions, for

both an oxidizing and reducing environment. Because cysteines are widely distributed in Nups (Figure S1), and disulfide bonds may be formed at intra-molecular, intra-subunit, intra-sub-complex, and inter-sub-complex levels. A large number of bonds at different levels are supposed to contribute to the integrated control of the NPC function.

Furthermore, the redox sensitivities of individual Nups correlate with their molecular properties, based on the hydrodynamic dimensions of FG-Nups (Yamada et al., 2010). Nups with small dimensions, such as Nup 50 and Nup 54, are found to be involved in the DTT-sensitive decrease of molecular crowding, while larger Nups, such as Nup 62, 98, 153, and 214, tend to increase molecular crowding in response to H_2O_2. In addition, the redox-insensitive Nup 58 is one of the Nups with the smallest hydrodynamic dimensions. Therefore, we speculate that different roles of Nups in responding to different redox conditions derive from their different hydrodynamic behaviors: Nups with different structural properties tend to work cooperatively to control the function of the NPC.

In addition, the redox-sensitive cysteines are evolutionally conserved among species. Based on the multiple protein sequence alignment for higher vertebrates, both cysteine residues in Nup 62 are conserved among species. In the case of the cysteine-enriched region of Nup 153 (C585–C874 of human Nup 153, which contains four zinc-finger domains), 18 cysteine residues out of a total of 21 residues are conserved among species (Figure S6). Cysteine-containing zinc-finger domain has been featured as a redox sensor that releases Zn ion and forms disulfide bonds under oxidative stress, as revealed in a redox-sensitive molecular chaperone Hsp33 (Graumann et al., 2001; Ilbert et al., 2007), DNA repair protein XPA (Witkiewicz-Kucharczyk et al., 2020), prokaryotic polymerase regulator DksA (Henard et al., 2014), and bacterial recombination protein RecR (Tang et al., 2014). Considering the property of the Nup 153 zinc-finger region as a major Ran-binding site, cysteine residues in Nup 153 may play a dual role in redox response: controlling both crowding states and Ran dynamics. Further studies focusing on the molecular structure and binding partners of CS-mutated Nup 153 under different redox conditions will clarify how Nup 153 balances its function.

Transport Regulation by the Degree of Crowding

Permeability of the nuclear pore is decreased under oxidative stress. In our FRAP experiments, a dose-dependent inhibition of nuclear transport of importin β was observed while cells were subjected to different concentrations of H_2O_2 (Figures 3H and 3I). The crowding states of individual Nups were directly linked to the NPC permeability, because overexpression of CS-mutated Nups partly abolished the dose-dependent transport inhibition.

Single-molecule fluorescence measurement revealed that oxidized and highly crowded NPCs held transport molecules longer inside, whereas reduced less-crowded NPCs became more accessible for the transport of molecules (Figure 4). Nup 50, one of the reducing condition-sensitive Nups, is involved in the effective release of the transit cargo-importin α/β complex (Sun et al., 2013). Because Nup 50 interacts with both importin α and β and serves as a docking site for the cargo-importin α/β complex within the pore, it is reasonable to assume that more molecules could reach Nup 50 if the molecular crowding state around Nup 50 was relaxed under reducing conditions. The observations that nuclear import of both importins was similarly and drastically affected by the oxidative stress support this idea (Figure 3K). However, longer retention within the NPC under oxidizing conditions may simply reflect the more densely formed crowding barrier that requires more time for migrating molecules to pass. Considering the special localization of oxidation-sensitive Nups throughout the NPC (Figure 5), oxidative stress may induce global structural changes of the NPCs to adopt a more compact conformation, leading to an increase in the molecular crowding states of the barrier.

A recent physical simulation of the NPC barrier by a coarse-grained model suggested that the increase in cohesiveness among Nup-IDRs leads to the decrease in their permeability (Gu et al., 2019). Our findings and proximal control model provide molecular insights of how cohesiveness is actually controlled *in vivo*: dynamic control at "sensor" regions leads to the spatial limitation for "effector" regions to alter FG-Nup's grafting density and eventually control the NPC permeability. There is no energy cost for this adaptive regulation system because the entire system is designed to be triggered by spontaneously formed disulfide bonds. The mechanism of the nuclear transport regulation by the crowding regulation serves as a model case for phase separation dynamics *in vivo*, which provides insights into the cellular strategy to orchestrate molecular activities at low-energy cost.

STAR★METHODS

Detailed methods are provided in the online version of this paper and include the following:

- KEY RESOURCES TABLE
- RESOURCE AVAILABILITY
  - Lead Contact
  - Materials Availability
  - Data and Code Availability
- EXPERIMENTAL MODEL AND SUBJECT DETAILS
- METHOD DETAILS
  - DNA construction, transfection, and Cell treatment
  - Observation and Quantification of FRET Ratio
  - Single NPC GimRET Analysis
  - Fluorescence recovery after photobleaching (FRAP) Assay
  - Setup for Single-molecule Fluorescence Observation
  - Analysis for Single-molecule Fluorescence Observation
  - Western blot Analysis
  - Co-precipitation Assay
- QUANTIFICATION AND STATISTICAL ANALYSIS

SUPPLEMENTAL INFORMATION

Supplemental Information can be found online at https://doi.org/10.1016/j.celrep.2020.108484.

ACKNOWLEDGMENTS

We thank Dr. Ogheneochukome Lolodi and Suguru Asai for technical support and discussions. This work was supported by a Grant-in-Aid for Scientific Research on Innovative Areas (24115512 to M.K.) from the Ministry of Education, Culture, Sports, Science and Technology, Japan and a Cross-Disciplinary Research Promotion Project (to M.K. and T.F.) from WPI-iCeMS, Kyoto University.

AUTHOR CONTRIBUTIONS

M.K. designed the study and directed the research. W.Z. performed single/bulk NPC GimRET measurements, CS mutation experiments, FRAP, and data analyses. R.W. performed bulk GimRET measurements and single-molecule fluorescence nuclear transport assays and their data analyses. H.A.K. contributed to the preparation of GimRET DNA constructs and data analysis. T.F. contributed to establishing the single-molecule fluorescence measurement system and data analysis. S.H.Y. contributed to the experimental design, data analysis, and discussions. All the authors contributed to the manuscript preparation.

DECLARATION OF INTERESTS

The authors declare no competing interests.

Received: January 15, 2020
Revised: September 1, 2020
Accepted: November 13, 2020
Published: December 15, 2020

REFERENCES

Aramburu, I.V., and Lemke, E.A. (2017). Floppy but not sloppy: Interaction mechanism of FG-nucleoporins and nuclear transport receptors. Semin. Cell Dev. Biol. *68*, 34–41.

Celetti, G., Paci, G., Caria, J., VanDelinder, V., Bachand, G., and Lemke, E.A. (2020). The liquid state of FG-nucleoporins mimics permeability barrier properties of nuclear pore complexes. J. Cell Biol. *219*, e201907157.

Cheezum, M.K., Walker, W.F., and Guilford, W.H. (2001). Quantitative comparison of algorithms for tracking single fluorescent particles. Biophys. J. *81*, 2378–2388.

Chug, H., Trakhanov, S., Hülsmann, B.B., Pleiner, T., and Görlich, D. (2015). Crystal structure of the metazoan Nup62•Nup58•Nup54 nucleoporin complex. Science *350*, 106–110.

Crampton, N., Kodiha, M., Shrivastava, S., Umar, R., and Stochaj, U. (2009). Oxidative stress inhibits nuclear protein export by multiple mechanisms that target FG nucleoporins and Crm1. Mol. Biol. Cell *20*, 5106–5116.

Denning, D.P., Patel, S.S., Uversky, V., Fink, A.L., and Rexach, M. (2003). Disorder in the nuclear pore complex: the FG repeat regions of nucleoporins are natively unfolded. Proc. Natl. Acad. Sci. USA *100*, 2450–2455.

Doucet, C.M., Esmery, N., de Saint-Jean, M., and Antonny, B. (2015). Membrane Curvature Sensing by Amphipathic Helices Is Modulated by the Surrounding Protein Backbone. PLoS ONE *10*, e0137965.

Elad, N., Maimon, T., Frenkiel-Krispin, D., Lim, R.Y., and Medalia, O. (2009). Structural analysis of the nuclear pore complex by integrated approaches. Curr. Opin. Struct. Biol. *19*, 226–232.

Fischer, J., Teimer, R., Amlacher, S., Kunze, R., and Hurt, E. (2015). Linker Nups connect the nuclear pore complex inner ring with the outer ring and transport channel. Nat. Struct. Mol. Biol. *22*, 774–781.

Frey, S., and Görlich, D. (2007). A saturated FG-repeat hydrogel can reproduce the permeability properties of nuclear pore complexes. Cell *130*, 512–523.

Frey, S., Richter, R.P., and Görlich, D. (2006). FG-rich repeats of nuclear pore proteins form a three-dimensional meshwork with hydrogel-like properties. Science *314*, 815–817.

García-Yagüe, A.J., Rada, P., Rojo, A.I., Lastres-Becker, I., and Cuadrado, A. (2013). Nuclear import and export signals control the subcellular localization of Nurr1 protein in response to oxidative stress. J. Biol. Chem. *288*, 5506–5517.

Graumann, J., Lilie, H., Tang, X., Tucker, K.A., Hoffmann, J.H., Vijayalakshmi, J., Saper, M., Bardwell, J.C., and Jakob, U. (2001). Activation of the redox-regulated molecular chaperone Hsp33–a two-step mechanism. Structure *9*, 377–387.

Grünwald, D., and Singer, R.H. (2012). Multiscale dynamics in nucleocytoplasmic transport. Curr. Opin. Cell Biol. *24*, 100–106.

Gu, C., Vovk, A., Zheng, T., Coalson, R.D., and Zilman, A. (2019). The Role of Cohesiveness in the Permeability of the Spatial Assemblies of FG Nucleoporins. Biophys. J. *116*, 1204–1215.

Hakim, A., Barnes, P.J., Adcock, I.M., and Usmani, O.S. (2013). Importin-7 mediates glucocorticoid receptor nuclear import and is impaired by oxidative stress, leading to glucocorticoid insensitivity. FASEB J. *27*, 4510–4519.

Henard, C.A., Tapscott, T., Crawford, M.A., Husain, M., Doulias, P.-T., Porwollik, S., Liu, L., McClelland, M., Ischiropoulos, H., and Vázquez-Torres, A. (2014). The 4-cysteine zinc-finger motif of the RNA polymerase regulator DksA serves as a thiol switch for sensing oxidative and nitrosative stress. Mol. Microbiol. *91*, 790–804.

Ilbert, M., Horst, J., Ahrens, S., Winter, J., Graf, P.C.F., Lilie, H., and Jakob, U. (2007). The redox-switch domain of Hsp33 functions as dual stress sensor. Nat. Struct. Mol. Biol. *14*, 556–563.

Kaminski, T., Siebrasse, J.P., Gieselmann, V., Kubitscheck, U., and Kappler, J. (2008). Imaging and tracking of single hyaluronan molecules diffusing in solution. Glycoconj. J. *25*, 555–560.

Kelley, K., Knockenhauer, K.E., Kabachinski, G., and Schwartz, T.U. (2015). Atomic structure of the Y complex of the nuclear pore. Nat. Struct. Mol. Biol. *22*, 425–431.

Kim, S.J., Fernandez-Martinez, J., Nudelman, I., Shi, Y., Zhang, W., Raveh, B., Herricks, T., Slaughter, B.D., Hogan, J.A., Upla, P., et al. (2018). Integrative structure and functional anatomy of a nuclear pore complex. Nature *555*, 475–482.

Konishi, H.A., and Yoshimura, S.H. (2020). Interactions between non-structured domains of FG- and non-FG-nucleoporins coordinate the ordered assembly of the nuclear pore complex in mitosis. FASEB J. *34*, 1532–1545.

Konishi, H.A., Asai, S., Watanabe, T.M., and Yoshimura, S.H. (2017). In vivo analysis of protein crowding within the nuclear pore complex in interphase and mitosis. Sci. Rep. *7*, 5709.

Kosako, H., Yamaguchi, N., Aranami, C., Ushiyama, M., Kose, S., Imamoto, N., Taniguchi, H., Nishida, E., and Hattori, S. (2009). Phosphoproteomics reveals new ERK MAP kinase targets and links ERK to nucleoporin-mediated nuclear transport. Nat. Struct. Mol. Biol. *16*, 1026–1035.

Kosinski, J., Mosalaganti, S., von Appen, A., Teimer, R., DiGuilio, A.L., Wan, W., Bui, K.H., Hagen, W.J., Briggs, J.A., Glavy, J.S., et al. (2016). Molecular architecture of the inner ring scaffold of the human nuclear pore complex. Science *352*, 363–365.

Li, C., Goryaynov, A., and Yang, W. (2016). The selective permeability barrier in the nuclear pore complex. Nucleus *7*, 430–446.

Lim, R.Y., Fahrenkrog, B., Köser, J., Schwarz-Herion, K., Deng, J., and Aebi, U. (2007). Nanomechanical basis of selective gating by the nuclear pore complex. Science *318*, 640–643.

Lin, D.H., Stuwe, T., Schilbach, S., Rundlet, E.J., Perriches, T., Mobbs, G., Fan, Y., Thierbach, K., Huber, F.M., Collins, L.N., et al. (2016). Architecture of the symmetric core of the nuclear pore. Science *352*, aaf1015.

Lowe, A.R., Tang, J.H., Yassif, J., Graf, M., Huang, W.Y., Groves, J.T., Weis, K., and Liphardt, J.T. (2015). Importin-β modulates the permeability of the nuclear pore complex in a Ran-dependent manner. Elife *4*, e04052.

Mészáros, N., Cibulka, J., Mendiburo, M.J., Romanauska, A., Schneider, M., and Köhler, A. (2015). Nuclear pore basket proteins are tethered to the nuclear envelope and can regulate membrane curvature. Dev. Cell *33*, 285–298.

Milles, S., Mercadante, D., Aramburu, I.V., Jensen, M.R., Banterle, N., Koehler, C., Tyagi, S., Clarke, J., Shammas, S.L., Blackledge, M., et al. (2015). Plasticity

of an ultrafast interaction between nucleoporins and nuclear transport receptors. Cell *163*, 734–745.

Mohr, D., Frey, S., Fischer, T., Güttler, T., and Görlich, D. (2009). Characterisation of the passive permeability barrier of nuclear pore complexes. EMBO J. *28*, 2541–2553.

Morikawa, T.J., Fujita, H., Kitamura, A., Horio, T., Yamamoto, J., Kinjo, M., Sasaki, A., Machiyama, H., Yoshizawa, K., Ichimura, T., et al. (2016). Dependence of fluorescent protein brightness on protein concentration in solution and enhancement of it. Sci. Rep. *6*, 22342.

Napetschnig, J., Blobel, G., and Hoelz, A. (2007). Crystal structure of the N-terminal domain of the human protooncogene Nup214/CAN. Proc. Natl. Acad. Sci. USA *104*, 1783–1788.

Otsuka, S., Iwasaka, S., Yoneda, Y., Takeyasu, K., and Yoshimura, S.H. (2008). Individual binding pockets of importin-beta for FG-nucleoporins have different binding properties and different sensitivities to RanGTP. Proc. Natl. Acad. Sci. USA *105*, 16101–16106.

Partridge, J.R., and Schwartz, T.U. (2009). Crystallographic and biochemical analysis of the Ran-binding zinc finger domain. J. Mol. Biol. *391*, 375–389.

Patel, V.P., and Chu, C.T. (2011). Nuclear transport, oxidative stress, and neurodegeneration. Int. J. Clin. Exp. Pathol. *4*, 215–229.

Raveh, B., Karp, J.M., Sparks, S., Dutta, K., Rout, M.P., Sali, A., and Cowburn, D. (2016). Slide-and-exchange mechanism for rapid and selective transport through the nuclear pore complex. Proc. Natl. Acad. Sci. USA *113*, E2489–E2497.

Ren, Y., Seo, H.S., Blobel, G., and Hoelz, A. (2010). Structural and functional analysis of the interaction between the nucleoporin Nup98 and the mRNA export factor Rae1. Proc. Natl. Acad. Sci. USA *107*, 10406–10411.

Sahli, L., Renard, D., Solé-Jamault, V., Giuliani, A., and Boire, A. (2019). Role of protein conformation and weak interactions on γ-gliadin liquid-liquid phase separation. Sci. Rep. *9*, 13391.

Sanulli, S., Trnka, M.J., Dharmarajan, V., Tibble, R.W., Pascal, B.D., Burlingame, A.L., Griffin, P.R., Gross, J.D., and Narlikar, G.J. (2019). HP1 reshapes nucleosome core to promote phase separation of heterochromatin. Nature *575*, 390–394.

Schrader, N., Koerner, C., Koessmeier, K., Bangert, J.A., Wittinghofer, A., Stoll, R., and Vetter, I.R. (2008). The crystal structure of the Ran-Nup153ZnF2 complex: a general Ran docking site at the nuclear pore complex. Structure *16*, 1116–1125.

Sun, C., Fu, G., Ciziene, D., Stewart, M., and Musser, S.M. (2013). Choreography of importin-α/CAS complex assembly and disassembly at nuclear pores. Proc. Natl. Acad. Sci. U S A *110*, E1584–E1593.

Tang, Q., Liu, Y.-P., Yan, X.-X., and Liang, D.-C. (2014). Structural and functional characterization of Cys4 zinc finger motif in the recombination mediator protein RecR. DNA Repair (Amst) *24*, 10–14.

Tetenbaum-Novatt, J., and Rout, M.P. (2010). The mechanism of nucleocytoplasmic transport through the nuclear pore complex. Cold Spring Harb. Symp. Quant. Biol. *75*, 567–584.

Timney, B.L., Raveh, B., Mironska, R., Trivedi, J.M., Kim, S.J., Russel, D., Wente, S.R., Sali, A., and Rout, M.P. (2016). Simple rules for passive diffusion through the nuclear pore complex. J. Cell Biol. *215*, 57–76.

Tokunaga, M., Imamoto, N., and Sakata-Sogawa, K. (2008). Highly inclined thin illumination enables clear single-molecule imaging in cells. Nat. Methods *5*, 159–161.

Vollmer, B., Schooley, A., Sachdev, R., Eisenhardt, N., Schneider, A.M., Sieverding, C., Madlung, J., Gerken, U., Macek, B., and Antonin, W. (2012). Dimerization and direct membrane interaction of Nup53 contribute to nuclear pore complex assembly. EMBO J. *31*, 4072–4084.

Witkiewicz-Kucharczyk, A., Goch, W., Olędzki, J., Hartwig, A.A.-O., and Bal, W. (2020). The Reactions of H(2)O(2) and GSNO with the Zinc Finger Motif of XPA. Not A Regulatory Mechanism, But No Synergy with Cadmium Toxicity. Molecules *25*, 4177.

Yamada, J., Phillips, J.L., Patel, S., Goldfien, G., Calestagne-Morelli, A., Huang, H., Reza, R., Acheson, J., Krishnan, V.V., Newsam, S., et al. (2010). A bimodal distribution of two distinct categories of intrinsically disordered structures with separate functions in FG nucleoporins. Mol. Cell. Proteomics *9*, 2205–2224.

Yoshimura, S.H., Otsuka, S., Kumeta, M., Taga, M., and Takeyasu, K. (2013). Intermolecular disulfide bonds between nucleoporins regulate karyopherin-dependent nuclear transport. J. Cell Sci. *126*, 3141–3150.

Zilman, A. (2018). Aggregation, Phase Separation and Spatial Morphologies of the Assemblies of FG Nucleoporins. J. Mol. Biol. *430*, 4730–4740.

STAR★METHODS

KEY RESOURCES TABLE

REAGENT or RESOURCE	SOURCE	IDENTIFIER
Cell Culture		
HeLa S3 cells	CCL-2.2, ATCC	HeLa
Dulbecco's Modified Eagle's Medium	Sigma	Cat. #D6046
Dulbecco's Modified Eagle's Medium, (-) Phenol Red	Sigma	Cat. #D5921
D-PBS(-)	Nacalai tesque	Cat. #14249-24
Fetal bovine serum	GIBCO/Sigma	Cat. #173012
Penicillin-Streptomycin Mixed solution	Nacalai tesque	Cat. #26253-84
L-glutamine solution	Sigma	Cat. #G7513
HEPES solution	Sigma	Cat. #H0887
Antibody		
anti-NPC antibody mAb414	Abcam	Cat. #ab24609; RRID:AB_448181
Anti-Ran antibody	BD	Cat. #610340; RRID:AB_397730
Rabbit polyclonal anti-GFP antibody	MBL	Cat. #598; RRID:AB_591819
Goat anti-Rabbit IgG(H+L), HRP	ThermoFisher	Cat. #A27036; RRID:AB_2536099
Goat anti-Mouse IgG(H+L), HRP	ThermoFisher	Cat. #A28177; RRID:AB_2536163
Chemicals		
CH_3COONa	Nacalai tesque	Cat. #31119-65
CH_3COOK	Nacalai tesque	Cat. #28405-05
$(CH_3COO)_2Mg$	Nacalai tesque	Cat. #20849-45
Diethylmaleate (DEM)	Alexis	Cat. #280-017
Digitonin	WAKO	Cat. #043-21371
DTT	Nacalai tesque	Cat. #14112-52
EGTA	Sigma (Fluka)	Cat. #03777
Glycine	Nacalai tesque	Cat. #17109-35
H_2O_2	Nacalai tesque	Cat. #18411-25
HEPES	Nacalai tesque	Cat. #17546-05
N-ethylmaleimide (NEM)	Nacalai tesque	Cat. #15512-11
PolyAcrylamide solution	Nacalai tesque	Cat. #06141-35
Sodium Lauryl Sulfate (SDS)	Nacalai tesque	Cat. #08933-05
Tris(hydroxymethyl)aminomethane)	Nacalai tesque	Cat. #35434-21
Triton X-100	Nacalai tesque	Cat. #28229-25
Protease inhibitor cocktail 100x	Nacalai tesque	Cat. #25955-11
PEI-MAX	Polysciences	Cat. #24765-1
Anti-GFP(Rat IgG2a), Monoclonal(GF090R), CC, Agarose Conjugate beads	Nacalai tesque	Cat. #06083-05
Commercial Kit		
Can Get Signal® Immunoreaction Enhancer Solution	TOYOBO	Cat. #NKB-101
Effectene® transfection reagent	QIAGEN	Cat. #301425
In-Fusion®HD Cloning Kit	Takara	Cat. #639649
KOD-Plus-Neo	TOYOBO	Cat. #KOD-401
Lipofectamine3000 transfection reagent	ThermoFisher	Cat. #L3000015

(*Continued on next page*)

Continued

REAGENT or RESOURCE	SOURCE	IDENTIFIER
Oligonucleotides		
See Tables S1 and S2 for the oligonucleotide sequences		
Recombinant DNA Constructs		
GimRET-Nup50	Konishi et al., 2017	Nup50
GimRET-Nup54	Konishi et al., 2017	Nup54
GimRET-Nup58	Konishi et al., 2017	Nup58
GimRET-rNup62	Konishi et al., 2017	Nup62
GimRET-Nup98	Konishi et al., 2017	Nup98
GimRET-Nup153	Konishi et al., 2017	Nup153
GimRET-Nup160	Konishi et al., 2017	Nup160
GimRET-Nup214	Konishi et al., 2017	Nup214
GimRET-Nup358	Konishi et al., 2017	Nup358
GimRET-Pom121	Konishi et al., 2017	Pom121
GimRET-Nup62CS	This study	Nup62CS
GimRET-Nup153CS	This study	Nup153CS
GimRET-Nup98CS	This study	Nup98CS
GimRET-Nup214CS	This study	Nup214CS
pEGFP-Nup62WT	This study	pEGFP-Nup62WT
pEGFP-Nup62CS	This study	pEGFP-Nup62CS
pEGFP-Nup153WT	This study	pEGFP-Nup153WT
pEGFP-Nup153CS	This study	pEGFP-Nup153CS
Synthetic DNA (CS Mutants)		
Nup153 (C585 to C874)	FASMAC	N/A
Nup214 (C102 to C299)	FASMAC	N/A
Software		
Fiji ImageJ	Fiji	ImageJ

RESOURCE AVAILABILITY

Lead Contact

Further information and requests for resources and reagents should be directed to the Lead Contact, Masahiro Kumeta (kumeta@lif.kyoto-u.ac.jp)

Materials Availability

All materials generated in this study are available from the Lead Contact without restriction

Data and Code Availability

This study did not generate datasets.

EXPERIMENTAL MODEL AND SUBJECT DETAILS

HeLa S3 cells (CCL-2.2, ATCC) were cultured in Dulbecco's Modified Eagle's Medium (DMEM, Sigma) supplemented with 10% fetal bovine serum (FBS, GIBCO/Sigma).

METHOD DETAILS

DNA construction, transfection, and Cell treatment

The construction of the crowding-sensitive FRET biosensor GimRET was described previously (Morikawa et al., 2016). Full-length cDNAs encoding human Nups 50, 54, and 58, were amplified from HeLa cell mRNA by RT-PCR. Other fragments and cDNAs encoding rat Nup 62 and human Nup 153 (kind gifts from K. Ullman, University of UTAH), human Nup 98 (a kind gift from T. Haraguchi, Advanced ICT research center), human Nup 160 (a kind gift from B. Fahrenkrog, University of Basel), human Nup 214, 358, and

rat Pom121 (kind gifts from J. Ellenberg, EMBL), were sub-cloned into the GimRET vectors as previously described (Konishi et al., 2017). The CS-mutated cDNA fragments for human Nup 153 (C585 to C874) and human Nup 214 (C102 to C299) were synthesized commercially (FASMAC). These fragments and host plasmid DNA were amplified by PCR and fused by using an In-Fusion cloning kit (Takara). The WT and CS mutants of pEGFP-Nup 62 and pEGFP- Nup 153 were subcloned from the respective GimRET constructions into the vector pEGFP-C1. For plasmid DNA transfection, Effectene transfection reagent (QIAGEN) was used to introduce DNAs 30 h before the experiments. To knockdown Nup 153, siRNA targeting 3′ untranslated region of human Nup 153 mRNA (ThermoFisher) was introduced into HeLa cells by Lipofectamine3000 transfection reagent (ThermoFisher). For the rescue condition, siRNA was first transfected to HeLa cells 48 h before the experiment, followed by the plasmid transfection 30 h before the experiment. To introduce oxidative stress, cells were treated with 2 mM H_2O_2 in culture medium for 1 h. For live cell microscopic observation, the medium without phenol red was used.

Observation and Quantification of FRET Ratio

HeLa cells expressing GimRET-fused Nups with or without H_2O_2 treatment were semi-permeabilized with digitonin (40 μg/mL) in transport buffer (20 mM HEPES-KOH, pH 7.3, 110 mM CH_3COOK, 2 mM $(CH_3COO)_2Mg$, 5 mM CH_3COONa, 0.5 mM EGTA, and 1 mM DTT), as described previously (Yoshimura et al., 2013). After digitonin treatment, the cells were washed twice with transport buffer with various concentrations of DTT (reduced conditions) or without DTT (oxidized condition) and incubated with the same buffer for 10 min at 37°C. Microscopy was performed using an FV1200 confocal laser-scanning microscope (Olympus) with a 60 × NA1.35 objective lens. The excitation wavelength was 433 nm, and the emission wavelength was between 460 to 500 nm for the CFP channel, and 520 to 570 nm for the FRET channel. For the bulk measurement, averaged signal intensities of the nuclear envelope and cytoplasm were quantified using ImageJ software (Version1.51W).

Single NPC GimRET Analysis

FRET signals were acquired for a part of the nucleus expressing GimRET-Nups. Image processing was performed with ImageJ software (Version1.51W). To identify the position of the NPC, maximum signal points were detected after enhancing the contrast, smoothing, and masking the areas other than the nuclear membrane within the CFP fluorescence image (Figure S7A). X-Y coordinates of the NPC position were recorded. Circular regions of interest (ROI) with a diameter of 7 pixels (∼190 nm) were set for the NPC positions. The sum of the CFP and YFP signals within the ROI, and the raw FRET ratio values were calculated. Accuracy of the single NPC detection was evaluated by overlaying immunostaining signal for NPC. GimRET-Nup expressing HeLa cells were immunostained by mAb414. Both GimRET and mAb414 signals were processed to detect spots on nuclear membrane. The analysis using GimRET-Nup 58 is shown (Figure S7B). The total number of spots detected from the same set of samples was 174 for GimRET and 485 for mAb414. Among the 174 GimRET spots, 160 (92.0%) of them were colocalized with mAb414 spots.

Fluorescence recovery after photobleaching (FRAP) Assay

Plasmid DNAs (pEGFP-Nup WT/CS, mCherry-importin β1, pEGFP-fused nuclear shuttling proteins) were transfected into HeLa cells using Effectene transfection reagent (QIAGEN). Microscopic observations were performed 24 h after transfection. DMEM containing 10% FBS and 10 mM HEPES (4-(2-hydroxyethyl)-1-piperazineethanesulfonic acid), without phenol red, was used to culture the HeLa cells for 1 h before observation. For the time-lapse imaging of FRAP, photobleaching, observation, and image acquisition were performed with a confocal laser scanning microscope (Olympus FV 1200) with a 60 × NA1.35 objective lens. The microscope sample chamber was maintained at 37°C throughout the experiments. For H_2O_2-stressed cells, time-lapse observation of FRAP was carried out within 30 min after the 1 h incubation with H_2O_2. The wavelength for photobleach and recording was 559 nm. Three images were acquired before bleaching, and all post-bleaching images were acquired with 1% laser intensity to reduce the loss of fluorescence intensity. The entire nucleus was photo-bleached at maximum output for 10 s (mCherry-importin β1). Nuclear fluorescence recovery images were captured every 5 s for 150 s. Fluorescence recovery was expressed as fluorescence intensity relative to maximum recovered intensity. Curve fitting and other kinetic analyses of the collected data were performed using Origin software (Light Stone), with the following fitting functions: $y = \exp(-xk_{out})Y_0+(k_{in}/k_{out})(1-\exp(-xk_{out}))$.

Setup for Single-molecule Fluorescence Observation

To obtain fluorescent labeled importin β1, a cDNA encoding human importin β1 was amplified by PCR from a HeLa single-stranded DNA pool. The amplified fragment was then inserted into the SacII and NotI sites of the vector pH6HTN His6HaloTag-T7 (Promega) to produce hexahistadine (His6)-tagged Halo-importin β1 for expression in BL21-CodonPlus-RIL Escherichia coli. Protein expression was induced by 1 mM isopropyl thiogalactoside (IPTG), and the protein was purified from *E. coli* lysates with Nickel beads, using a gradient of 30–250 mM imidazole for the elution. Purified recombinant Halo-importin β1 was then labeled with 2.5 μM HaloTag Tetramethyl Rhodamine (TMR) ligand (Promega). Excess dye was removed by Bio-Rad Bio-Spin Bio-Gel P6 or P30 columns (100 μL labeled protein/column) and the labeling efficiency was checked by a fluorescence scanner (Typhoon Variable Mode Imager 9400, GE Healthcare). For single-molecule fluorescence measurement of nuclear transport, HeLa cells were permeabilized with 40 μg/mL digitonin for 5 min on ice and preincubated with transport buffer with 10 mM DTT for 10 min prior to observation. For measurements under oxidizing conditions, cells were treated with 2 mM H_2O_2 for 1 h before the permeabilization, and preincubated with transport buffer without DTT. For reducing conditions, permeabilized cells were preincubated with transport buffer supplemented

with 100 mM DTT. A TIRF microscope (ELYRA P.1, Carl Zeiss) was set in a HILO mode by adjusting the angle of incidence of the excitation laser (Figure 4A), based on a method described previously (Tokunaga et al., 2008). 1 nM TMR-tagged Halo-importin β1 was then added, and 4,000 images were acquired at an exposure rate of 15 ms/frame for 60 s.

Analysis for Single-molecule Fluorescence Observation

First, the location of the NPC was identified. Image processing was performed by ImageJ software (Version1.51W). After subtracting background with the ImageJ standard rolling ball algorithm, 4,000 frames were spit into 80 sets of 50 frames. Standard deviations were calculated for each pixel in each of the sets, and constructed into the 50 frame SD image (Figure 4B). Since the SD image showed a better signal-to-noise ratio, this image was used to identify the fluorescence spots. For each of the SD images, fluorescent spots were detected by a Laplacian of Gaussian method (Cheezum et al., 2001; Kaminski et al., 2008). X-Y coordinates for the spots were recorded. Next, each retention event of importin β1 in the NPC was scored by setting a threshold for the fluorescence level. A region of interest (ROI) was set for each of the X-Y coordinates recorded, and the sum of the fluorescence intensity within the ROI (= single NPC) was obtained from every frame. Due to the bleaching of the fluorescence, a significant decrease of the background fluorescence level was observed (Figure S8A). To evaluate the event of fluorescence detection considering the differences in background level during the time-course, ten different time frames were set: 1,000-4,000 frames (orange), 1-1,000 / 1,001-2,000 / 2,001-3,000 / 3,001-4,000 frames (green), 1-500 / 501-1,500 / 1,501-2,500 / 2,501-3,500 / 3,500-4,000 frames (blue). In each time frame, a threshold line was set as (average of the lowest 90% signal intensities) + (5X SD of the lowest 90% signal intensities) (Figure S8A, colored lines). Among the overlapping threshold lines, the lowest value at each time point was set as the final threshold line (Figure S8B, red line). Signals higher than the final threshold line were scored as fluorescence detection events. To consider blinking of the fluorescence in long retention events, two spots detected within 15 frames were recognized as the continuous retention of a single fluorescent molecule, unless the fluctuation level between the two spots completely dropped to the background level (Figure S8C, arrowheads). The number of detected events and retention times were obtained for each NPC under different redox conditions (Figure 4).

Western blot Analysis

HeLa cells expressing GimRET-fused Nup 62 WT/CS or Nup 153 WT/CS were harvested 24 h after transfection. For oxidative condition, cells were treated with 2mM H_2O_2 containing DMEM for 1 h. Nuclear lysate was prepared by sequential treatment of cells with digitonin (40 μg/mL) for 5 min and 0.5% Triton-X, at 4°C. The nuclear fraction was collected by centrifugation (700 × g, 2 min at 4°C). The whole process was performed in the presence of a thiol-blocking reagent N-ethylmaleimide (NEM) to prevent the natural oxidation during sample preparation, as described previously (Yoshimura et al., 2013). 100 mM DTT was added to the reduced condition samples during SDS-PAGE sample preparation. SDS-PAGE loading buffer without DTT was used for standard and oxidative conditions. Anti-GFP antibody (MBL) and mAb414 (Abcam) were used for western blot. Can Get Signal® Immunoreaction Enhancer Solution (TOYOBO) was used to enhance weak signals when needed. Band intensities were quantified by using ImageJ software (Version1.51W).

Co-precipitation Assay

HeLa cells transfected with pEGFP-Nup 153 WT/CS using PEI-MAX® transfection reagent (Polysciences) were collected 30 h after transfection. The cell lysate was prepared by gentle sonication in pull-down buffer (20 mM HEPES (pH 7.4), 120 mM NaCl, 5 mM $MgCl_2$, 2 mM EGTA, 1 mM DTT and Protease inhibitor cocktail (Nacalai Tesque)), followed by the addition of 1.0% Triton X-100, incubated 20 min on ice, and centrifugation (20,000 xg, 20 min, 4°C). The anti-GFP (Rat IgG2a) monoclonal antibody conjugated agarose beads (Nacalai Tesque) were used for pull-down of exogenous pEGFP-Nup 153 WT/CS from the cell lysate, by overnight incubation. After 4 times of wash with pull-down buffer, the beads were collected and subjected to western blot. The Anti-GFP (MBL) and Anti-Ran (BD) antibodies were used for the detection of EGFP-Nup 153 WT/CS and co-precipitated Ran. Band intensities were quantified by using ImageJ software (Version1.51W).

QUANTIFICATION AND STATISTICAL ANALYSIS

All the statistical evaluation of the data was basically done by Welch's t test, unless otherwise noted.